RSC Advances

PAPER

View Article Online
View Journal | View Issue

Cite this: *RSC Adv.*, 2025, **15**, 30089

Hydrothermal synthesis of Fe_2O_3–Ag_2O nanocomposites supported on pristine, N/S doped graphene oxide for photocatalytic and biological applications

Safeena Zafar,[a] Bilal Ahmad Khan,*[a] Ikhtiar Ahmad,[ab] Muhammad Naeem Ahmed,[a] Rasool Khan,[c] Mahmoud A. A. Ibrahim,[de] Aroosa Zafar[f] and Sirajul Haq*[a]

Addressing the dual challenges of industrial contamination in wastewater and antimicrobial resistance is crucial for environmental preservation and global health, aligning with sustainable development goals. This study investigated the biological and photocatalytic potential of pure bimetal oxides, nanocomposites (NCs) and their counterparts incorporating graphene oxide (GO) and nitrogen- and sulfur-doped GO. A set of samples, namely Fe_2O_3–Ag_2O, Fe_2O_3–Ag_2O@GO, Fe_2O_3–Ag_2O@N-GO, and Fe_2O_3–Ag_2O@S-GO NCs, was synthesized using the hydrothermal method. The synthesized NCs underwent comprehensive structural and compositional analyses using XRD, FTIR, EDX, SEM, and UV-visible spectroscopy. Their photocatalytic performance was evaluated for methylene blue (MB) dye degradation under direct sunlight at varying pH levels, dye concentrations, and reaction times. The photocatalytic tests revealed a significant enhancement in methylene blue (MB) degradation efficiency, which generally increased with rising pH, albeit with some deviations. Among all samples, Fe_2O_3–Ag_2O@S-GO NC exhibited the highest photocatalytic activity, achieving maximum degradation at 240 min. The biological properties of NCs were assessed through protein kinase inhibition studies and antimicrobial assays, while hemocompatibility was determined *via* hemolytic activity. All samples exhibited both bacteriostatic and bactericidal effects, as indicated by the presence of a bald zone alongside a clear zone. The Fe_2O_3–Ag_2O NC demonstrated the most notable antibacterial activity, achieving the MIC of 12.5 against *S. aureus*. The antibacterial assay further demonstrated enhanced inhibitory effects against both resistant and non-resistant bacterial strains, confirming that iron- and silver-doped composites exhibited superior antibacterial properties. Among all the NCs, Fe_2O_3–Ag_2O@GO NC displayed significant antifungal activity against five different strains, with the highest effectiveness against *Aspergillus niger* and *Mucor*, achieving a zone of inhibition of 9 ± 0.01 mm. The hemolytic assay indicated that all NCs exhibited hemolysis levels below 1%, confirming their safety for biological applications. This study highlighted the potential of these NCs for enhancing the photocatalytic degradation of MB dye in water while also demonstrating their biological significance.

Received 29th July 2025
Accepted 4th August 2025

DOI: 10.1039/d5ra05475c

rsc.li/rsc-advances

1. Introduction

The rapid pace of industrialization and technological advancements, combined with inadequate environmental regulations, have resulted in the discharge of significant amounts of hazardous effluents into natural water bodies.[1] Azo dyes constitute a major portion of the waste generated by chemical, textile, petroleum, and other industries.[2] These toxic dyes pose serious threats not only to aquatic ecosystems but also to human health and terrestrial organisms. These are known to be mutagenic, carcinogenic, as well as highly detrimental to the central nervous system. Prolonged exposure to these substances can lead to respiratory issues, genetic disorders, cancer, chromosomal abnormalities, and various acute health problems.[3] Moreover, these dyes can persist in the environment for extended periods without degrading. Given this critical situation, it is imperative to minimize and eliminate these chemical pollutants, particularly synthetic dyes, from the ecosystem.[4]

[a]*Department of Chemistry, University of Azad Jammu and Kashmir, Muzaffarabad 13100, Pakistan. E-mail: cii_raj@yahoo.com*
[b]*Department of Chemistry, Women University, Bagh, Azad, Kashmir 12500, Pakistan*
[c]*Institute of Chemical Sciences, University of Peshawar, Peshawar, 25120, Pakistan*
[d]*Chemistry Department, Faculty of Science, Minia University, Minya 61519, Egypt*
[e]*School of Health Sciences, University of KwaZulu-Natal, Westville Campus, Durban 4000, South Africa*
[f]*Department of Pharmacy, Faculty of Biological Sciences, Quaid-i-Azam University, Islamabad, 45320, Pakistan*

Graphene and graphene-based materials have unique characteristics that make them extremely valuable in fields such as biology and environmental science. A recent development has attracted graphene based nanomaterials, demonstrating their applicability in a range of sustainable applications. Additionally, graphene oxide–semiconductor hybrid nanomaterials have been extensively employed for the photocatalytic degradation of antibiotics, organic dyes, pharmaceutical compounds, phenolic substances, as well as for photocatalytic hydrogen production and disinfection processes.[5,6] Various strategies have been explored to enhance the chemical activity and electrical properties of graphene derivatives.[7–9] Among these, doping has emerged as a highly effective technique for improving the photocatalytic degradation of organic and inorganic pollutants.[10] The chemical modification of graphene oxide with heteroatoms such as nitrogen and sulfur is recognized as a promising approach to enhancing its electrical and mechanical properties.[11] Nitrogen/sulfur-doped GO-based materials have gained significant attention due to their wider bandgap which arises from the electron-withdrawing effects of sulfur and nitrogen. These doped carbon-based materials exhibit exceptional catalytic activity. Furthermore, the incorporation of sulfur or nitrogen into GO sheets has been shown to significantly improve their electrical conductivity, making them highly suitable for the photocatalytic process.[12] Moreover, the incorporation of nitrogen (N) and sulfur (S) into graphene oxide (GO) significantly enhances its functional properties, making it a powerful material for catalytic, environmental, and biomedical applications. N/S doping introduces electron-rich sites, reducing GO's bandgap and improving charge carrier mobility. Moreover, the N/S atoms create defects and catalytic centers that boost photocatalytic degradation of pollutants *via* ROS generation ($^{\bullet}OH$, $^{\bullet}O_2^-$).

Protein phosphorylation, driven by protein kinase (PKA), represents a significant post-translational amendment that plays a vital role in pathways of cellular signaling.[13] Various clinical conditions are closely associated with irregular phosphorylation and PKA function.[14] The extensive exploration of protein kinases has positioned them as key targets in drug discovery and development efforts. Consequently, assessing PKA activity is essential for comprehending relevant biological processes, diagnosing diseases, and facilitating drug development.[15]

The rising prevalence of multidrug-resistant pathogens and the limited efficacy of conventional antimicrobial agents have necessitated the development of novel nanomaterials with enhanced biological activity. Nanosized Fe_2O_3 and Ag_2O have garnered significant attention due to their unique physicochemical properties, including high surface area, tunable bandgap, and excellent catalytic activity.[16,17] When combined to form bimetallic Fe_2O_3–Ag_2O NC, these materials exhibit enhanced functionalities, such as improved charge separation, synergistic catalytic effects, and superior redox properties, making them highly effective for applications in photocatalysis, sensing, and environmental remediation.[18,19] However, their standalone applications often face challenges, including aggregation, limited biocompatibility, and insufficient targeting efficiency. To address these limitations, integrating these nanomaterials with nitrogen/sulfur doped GO has been proposed, as N/S-GO can enhance dispersion, stability, and biocompatibility while introducing additional active sites for improved biological interactions.[12,20–22] The incorporation of GO not only improves the electrical conductivity and stability of the NC but also introduces additional active sites and defects that facilitate better adsorption and catalytic activity. This hybrid system, combining the advantages of bimetallic oxides and doped graphene oxide, represents a promising avenue for advanced materials with tailored properties for energy, environmental, and biomedical applications.[23] Despite these advancements, a comprehensive understanding of their antibacterial, antifungal, protein kinase inhibition, and hemolytic activities had remained underexplored.

This study aimed to systematically evaluate the biological efficacy of Fe_2O_3–Ag_2O NC and its N/S-GO doped counterparts, addressing critical gaps in their application for combating microbial infections, inhibiting cancer-related protein kinases, and assessing biocompatibility through hemolytic studies. Despite the potent properties of Fe_2O_3–Ag_2O, Fe_2O_3–Ag_2O@GO, Fe_2O_3–Ag_2O@N-GO, and, Fe_2O_3–Ag_2O@S-GO NCs, no comprehensive study had demonstrated their efficacy in environmental and biological applications. Therefore, the novelty of this project was in exploring the photocatalytic and biological potential of these bimetal oxide NCs, along with their N- and S-doped GO-based counterparts, and comparing them with typical GO-based materials and those without GO. The study explored and compared the biological and environmental applications of the synthesized NCs. It substantiated the potential of GO-based bimetallic iron and silver oxides doped with nitrogen and sulfur in wastewater treatment and biological efficacy improvements. The findings underscored the importance of continued research in this field for environmental and public health benefits.

2. Materials and methods

2.1 Reagents

To prepare required NCs, silver nitrate hexahydrate, iron(III) nitrate nonahydrate, ammonia, sodium sulphide, sulfuric acid (98%), potassium permanganate (0.1 N), potassium persulfate (5% (w/v)), hydrogen peroxide (30%), ethylene glycol (1.113 g mL^{-1} at 25 °C), sodium nitrate (15-N), graphite powder black (2.2 g mL^{-1} at 25 °C) and urea (powder) were used. These reagents were obtained from Sigma-Aldrich and used without further purification, prepared and applied as instructed by the supplier. Moreover, deionized water (DIW) was used to thoroughly wash the prepared NCs.

2.2 Synthesis of GO

An improved version of the Hummers' method, which involved specific modifications, was employed for the oxidation of graphite to synthesize GO.[24]

2.3 Synthesis of sulphur doped graphene (GS)

To prepare sulphur doped graphene (GS), 500 mg of GO was dissolved in DIW (100 mL) and kept in a sonicator for half an

hour. Afterward, 5 g of sodium sulphide (Na_2S) was slowly added while stirring and the mixture was sonicated again for half an hour. Then, entire mixture was transferred to a stainless steel autoclave lined with Teflon, where it was subjected to heating at 150 °C for 12 h. Once the autoclave reached ambient temperature, the blackish powdered material obtained was thoroughly washed with DIW and subsequently oven-dried at 60 °C.

2.4 Synthesis of nitrogen doped graphene (GN)

The synthesis of NG began by dissolving 1.12 g (4 mmol) of GO in distilled water, followed by 30 min of sonication. A mixture of this GO dispersion and urea (at a 1 : 300 mass ratio) was then prepared and ultrasonically stirred for 2 h at room temperature. The complete mixture was subsequently transferred to a 100 mL Teflon-lined stainless steel autoclave and held at 180 °C for 12 h. Following the high temperature phase, mixture was cooled to room temperature. After cooling, the prepared black powder was rinsed multiple times with DIW before being placed in an oven to dry overnight. After drying, the amount of the prepared nanomaterial was determined.

2.5 Synthesis of Fe_2O_3–Ag_2O NCs

A pre-determined amount of $Fe(NO_3)_3 \cdot 9H_2O$ and $AgNO_3 \cdot 6H_2O$ (1 : 1 molar ratio) was dissolved in distilled water under continuous stirring. A precipitating agent, NH_3 solution, was added dropwise to adjust the pH at 11. The homogeneous mixture was subsequently transferred to a 100 mL Teflon-lined stainless steel autoclave and heated at 140 °C for 6 h. Following cooling to room temperature, the precipitate was washed thoroughly with DIW, dried at 80 °C for 6 h, and then calcined at 380 °C in a muffle furnace to yield Fe_2O_3–Ag_2O NCs.

2.6 Synthesis of Fe_2O_3–Ag_2O@GO, Fe_2O_3–Ag_2O@N-GO, and Fe_2O_3–Ag_2O@S-GO NCs

Fe_2O_3–Ag_2O@GO, Fe_2O_3–Ag_2O@N-GO, and Fe_2O_3–Ag_2O@S-GO NCs were synthesized following separate but similar procedures. GO, GN, and GS (0.5 g each) were individually dispersed in DIW (10 mL) and ethylene glycol (20 mL), followed by sonication for 20 min to achieve homogeneity. Separately, $Fe(NO_3)_3 \cdot 9H_2O$ and $AgNO_3 \cdot 6H_2O$ (1 : 1 molar ratio) were dissolved in distilled water and added to each dispersion under constant stirring for 30 min. NH_3 solution was then added dropwise until the pH reached 11, ensuring proper precipitation of metal oxides onto the respective GO-based materials. The mixtures were then transferred into Teflon-lined stainless steel autoclaves and heated at 140 °C for 6 h. After cooling to room temperature, the resulting NCs were thoroughly washed with DIW and dried at 80 °C for 6 h. The dried sample was then subjected to calcination at 380 °C. The final products, Fe_2O_3–Ag_2O@GO, Fe_2O_3–Ag_2O@N-GO, and Fe_2O_3–Ag_2O@S-GO NCs, were weighed and stored in sealed vials for further characterization and application studies.

2.7 Instrumentation

To thoroughly characterize the prepared Fe_2O_3–Ag_2O, Fe_2O_3–Ag_2O@GO, Fe_2O_3–Ag_2O@N-GO, and, Fe_2O_3–Ag_2O@S-GO NCs, a series of physicochemical investigations was employed. In order to determine the maximum absorbance (λ) of prepared NCs, a UV-1601 SHIMADZU model spectrophotometer was used. By using FTIR-8400S SHIMADZU spectrophotometer, surface moieties between 4000 and 500 cm^{-1} were examined. For the quantification of crystallite size, the Debye–Scherrer equation was applied. The crystalline structure of the materials was characterized by XRD using a Philips X'Pert diffractometer. Surface morphology of all synthesized NCs was assessed with a JEOL/EO JSM-6510 scanning electron microscope (SEM) operating at 15 kV. Elemental composition was investigated through EDX spectroscopy, performed on a JSM-6490 (JEOL) system.

2.8 Photocatalytic assay

The photocatalytic activity of all the synthesized samples, consisting of Fe_2O_3–Ag_2O, Fe_2O_3–Ag_2O@GO, Fe_2O_3–Ag_2O@N-GO, and, Fe_2O_3–Ag_2O@S-GO NCs was assessed in the decomposition of MB. A 50 mg L^{-1} standard solution of MB was prepared using distilled water. Subsequently, 20 mg of the prepared catalyst samples were added to separate reaction vessels each containing 20 mL of this MB solution. To establish adsorption–desorption equilibrium, the mixtures were stirred in darkness for 30 min. Following this, the samples were exposed to simulated solar radiation for predefined time intervals, and their degradation was systematically monitored using a double beam UV-vis spectrophotometer. The variations in the absorbance maxima were monitored over time. Different parameters were checked such as the effect of pH, time and initial concentration.

2.8.1 pH study. The pH study was conducted by taking 20 mL dye solution at the concentration of 50 mg L^{-1} and 20 mg catalyst. The beaker was marked to the point where the stirrer was submerged in the solution as the reference point was used to add DIW to compensate for water loss due to accelerated evaporation due to sunlight. The study was carried out by adjusting the pH of the dye solution using 0.1 M NaOH and 0.1 M HCl, with the pH range selected between 4 and 11. The samples were analyzed using a double-beam spectrophotometer to determine the optimum pH.

2.8.2 Kinetic study. The kinetic study was conducted by taking a 100 mL solution of the dye at a concentration of 50 mg L^{-1} and a 100 mg catalyst. The beaker was marked to the point where the stirrer was submerged in the solution as this reference point was used to add DIW to compensate for water loss due to accelerated evaporation under sunlight. The study was conducted using the finite bath method. The sample were taken at different time intervals and was analyzed using a double-beam spectrophotometer to determine the optimum time.

2.8.3 Concentration study. The concentration study was conducted by taking a 20 mL solution of the dye at different concentrations ranging from 12.5 to 200 mg L^{-1}, with 20 mg of catalyst used. The beaker was marked to the point where the

stirrer was submerged in the solution and this reference point was used to add DIW to compensate for the water loss due to accelerated evaporation due to sunlight. The samples were analyzed using a double-beam spectrophotometer to find the optimum concentration.

2.9 Protein kinase inhibition assay

The inhibitory potential of NCs was evaluated using protein kinase derived from *Streptomyces* 85E strain. The *Streptomyces* 85E strain was cultured in tryptone soya broth media. Afterwards, the bacterial lawn was prepared by streaking a loopful of bacteria onto pre-sterilized Petri plates containing ISP4 media. A 5 mm disc impregnated with 20 μg of NCs was then placed on those prepared plates which were incubated for 72 h. The inhibitory effects were assessed by measuring the zone of inhibition (ZOI) in millimeters using a vernier caliper. The presence of clear and bald inhibition zones surrounding the nanocomposites and control discs was recorded to determine their inhibitory potential.

2.10 Antibacterial assay

Antibacterial potential of synthesized Fe_2O_3–Ag_2O, Fe_2O_3–Ag_2O@GO, Fe_2O_3–Ag_2O@N-GO, and, Fe_2O_3–Ag_2O@S-GO NCs were measured by micro broth dilution method against *Bacillus subtilis* (ATCC-6633), *Staphylococcus aureus* (ATCC-6538), *Klebsiella pneumoniae* (ATCC-1705), *Pseudomonas aeruginosa* (ATCC-15442) and *Escherichia coli* (ATCC-25922), as well as unaffected *Acinetobacter*, *MRSA* and *Escherichia coli*. Bacterial inoculum were prepared under sterile conditions, achieving a density of approximately 5×10^4 CFU mL^{-1} in pre autoclaved nutrient broth. A 5 μL aliquot of each test NC was added to the corresponding wells of a 96-well plate, followed by the addition of 195 μL of nutrient broth. Each test nanomaterial was serially diluted to attain final concentrations of 25, 12.5, 6.25, and 3.125 μg mL^{-1}. Ciprofloxacin served as the positive control, while DMSO was used as the negative control. Following the addition of samples and inoculum, the plates were incubated at 37 °C for 24 hours. The results were then evaluated to determine the minimum inhibitory concentration (MIC).[25]

2.11 Antifungal assay

The antifungal activity of the Fe_2O_3–Ag_2O, Fe_2O_3–Ag_2O/GO, Fe_2O_3–Ag_2O/N-GO and Fe_2O_3–Ag_2O/S-GO NCs against *Mucor* species (FCBP-0300), *Aspergillus fumigatus* (FCBP-66), *Fusarium solani* (FCBP-0291), *Aspergillus niger* (FCBP-0198) and *Aspergillus flavus* (FCBP-0064), and was evaluated using disc diffusion method.[31] Prior to use, fungal strains were suspended in a sterilized 0.02% Tween-20 solution. Pre-autoclaved Petri plates were taken and Sabouraud dextrose agar (SDA) was poured into them. Once solidified, 100 μL of each fungal suspension, adjusted to match the 0.5 McFarland turbidity standard, was evenly spread across the agar surface. Subsequently, sterile discs were impregnated with 5 μL of each NC sample (4 mg mL^{-1} in DMSO). Amphotericin B served as the positive control, while DMSO was used as the negative control. The plates were then incubated at 28 °C for 48 h. After incubation, the antifungal activity was assessed by measuring the average diameter of the inhibition zones (in mm) around the discs. These results were recorded and analysed to compare the effectiveness of the prepared NCs against the selected fungal strains.

2.12 Hemolytic assay

The hemolysis assay was done to evaluate the hemolytic potential of prepared samples using method existing in literature.[26] Initially, human donor blood was collected in an EDTA tube. Blood was first centrifuged at 10 000 rpm for 10 min to separate RBCs. The supernatant was then carefully removed, and the RBCs were washed three times with phosphate-buffered saline (PBS) to ensure complete removal of plasma and other components. A 5% RBC suspension was subsequently prepared by resuspending the washed cells in PBS. For the assay, 150 μL of each NC sample was added to separate Eppendorf tubes, followed by the addition of 350 μL of the RBC suspension. The Eppendorf tubes were incubated at 37 °C for 30 min. Following incubation, centrifugation was performed at 10 000 rpm for 5 min to pellet the intact RBCs. Finally, 200 μL of the supernatant from each tube was carefully transferred to a 96-well plate, and absorbance was measured at 530 nm using a spectrophotometer. The percentage of hemolysis was calculated by given formula.

$$\%\ \text{hemolysis} = \frac{A_s - A_{nc}}{A_{pc} - A_{nc}} \times 100$$

3. Results and discussion

3.1 XRD analysis

XRD analysis confirmed the successful synthesis of graphene oxide (GO), sulfur-doped GO (S-GO), and nitrogen-doped GO (N-GO) and the diffractograms (S1) are reported in our previous study (Zafar *et al.*,[24] 2024). Pure graphite showed a peak at $2\theta \approx 26°$, while GO exhibited a peak at $2\theta \approx 10.5°$, indicating oxidation and increased interlayer spacing due to oxygen functional groups. In the sulfur- and nitrogen-doped samples, this peak shifted to 25.3° and 24.2°, respectively, suggesting effective reduction of GO and successful doping under hydrothermal conditions (Kumar *et al.*,[26] 2020).

Fig. 1 displays the XRD patterns of Fe_2O_3–Ag_2O, Fe_2O_3–Ag_2O@GO, Fe_2O_3–Ag_2O@N-GO, and, Fe_2O_3–Ag_2O@S-GO NCs which exhibited characteristic peaks corresponding to the reference code 96-901-3477 (for Fe_2O_3 NPs) and reference code 96-901-2432 (for Ag_2O NPs). XRD data from Fe_2O_3–Ag_2O, Fe_2O_3–Ag_2O@GO, Fe_2O_3–Ag_2O@N-GO, and, Fe_2O_3–Ag_2O@S-GO NCs indicated that the composition of the 2θ diffraction features was dominant with matching Bragg's reflections at 37.21° (111), 44.50° (Fe_2O_3 011, GO 022), 65.61° (Fe_2O_3 002, GO 220) and 78.92° (Ag 113).[27–30] The assimilated oxides of metals demonstrated significant crystalline characteristics, and the XRD data aligned well with reference codes of both elements. In Fe_2O_3–Ag_2O@GO, Fe_2O_3–Ag_2O@N-GO, and, Fe_2O_3–Ag_2O@S-GO NCs, no carbon related diffraction peaks were detected. The presence

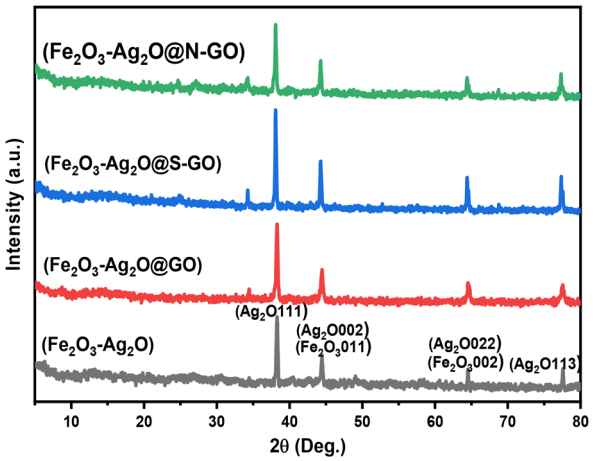

Fig. 1 XRD patterns of Fe_2O_3/Ag_2O, Fe_2O_3/Ag_2O/GO, Fe_2O_3/Ag_2O/S-GO and Fe_2O_3/Ag_2O/N-GO NCs.

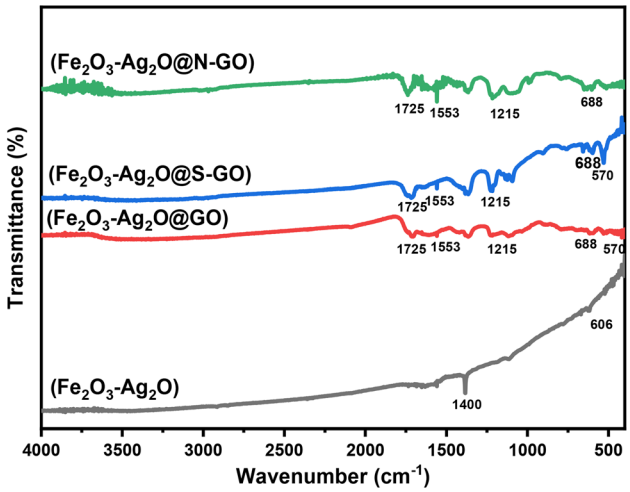

Fig. 2 FTIR spectra of Fe_2O_3/Ag_2O, Fe_2O_3/Ag_2O/GO, Fe_2O_3/Ag_2O/S-GO, Fe_2O_3/Ag_2O/N-GO NCs.

of magnetite might have been responsible for this, as it reduced the aggregation of graphene sheets resulting in the formation of more monolayer graphene.[31] Consequently, carbon peaks appeared weaker. Alternatively, this could have resulted from the overwhelming intensity of the strong signals from iron and silver oxides, which suppressed the weak carbon peaks in XRD data. This observation suggested that GO sheets were exfoliated due to the sufficient loading of NCs on their surfaces.[32] This study demonstrated that interaction between GO and NCs was very effective. The XRD crystallite size was estimated using Debye–Scherrer formula.[33] According to the calculations, Fe_2O_3–Ag_2O NC exhibited crystallite size of 58 nm while Fe_2O_3–Ag_2O@GO, Fe_2O_3–Ag_2O@S-GO, and Fe_2O_3–Ag_2O@N-GO NCs had 53 nm, 22 nm, and 39 nm, respectively.

3.2 FT-IR analysis

FTIR spectroscopy was used to identify functional groups in GO, S-GO, and N-GO, confirming the successful incorporation of oxygen, sulfur, and nitrogen functionalities (S2). GO showed characteristic peaks at 1725 cm^{-1} (C=O stretching), 1917 cm^{-1} (epoxy C–O–C), and broad C–O bands between 1000–1400 cm^{-1}, indicating carboxyl, epoxy, and hydroxyl groups. Peaks at 1571 and 1725 cm^{-1} correspond to C=C and C=O stretching in GO. In N-GO, reduced peak intensities suggest removal of oxygen groups during reduction. A peak at 1154 cm^{-1} confirms C–N bonding, and the 1558 cm^{-1} peak corresponds to altered C=C structure (Hamid *et al.*,[33] 2021). A broad peak around 3400 cm^{-1} indicates O–H stretching (Bibi *et al.*,[33] 2020). In S-GO, peaks at 1720 cm^{-1} and 1160 cm^{-1} represent –COOH and –C–O–C– groups, while peaks at 3420 and 1130 cm^{-1} confirm S–H and C–S vibrations, indicating successful sulfur doping (Haq *et al.*,[33] 2018).

Fig. 2 presents the FT-IR spectra, displaying distinct bands at various wavenumbers (cm^{-1}), which correspond to specific infrared radiation absorption events. Notably, the band observed at 1660 cm^{-1} is attributed to the bending vibrations of adsorbed water or hydroxyl groups.[34] The spectra revealed two strong absorption bands at 570 cm^{-1} and 688 cm^{-1}. These bands are attributed to the (Fe–O) stretching vibrations originating from the tetrahedral sites and the (Fe–O) torsional vibration mode of Fe in the octahedral sites of magnetite, respectively.[35] The bands at 1725 cm^{-1} for (C–O), 1553 cm^{-1} for aromatic (C–C), and 1215 cm^{-1} for epoxy (C–O) were observed in Fe_2O_3–Ag_2O@GO, Fe_2O_3–Ag_2O@S-GO, and Fe_2O_3–Ag_2O@N-GO, but not in Fe_2O_3–Ag_2O NC, confirming the synthesis of required NCs.[36] As the bands of all four prepared NCs were analyzed, shifts in various bands became evident. The intensity of certain bands gradually increased from Fe_2O_3–Ag_2O NC to its GO-, N-GO-, and S-GO-doped counterparts, reaching an even higher intensity in Fe_2O_3–Ag_2O@N-GO NCs. Additionally, some minor bands began to appear in these NCs. These shifts can primarily be attributed to the interactions between the metal oxides (Fe_2O_3 and Ag_2O) and graphene-based materials (GO, N-GO, S-GO), along with doping effects, surface plasmon resonance, and changes in crystallinity. These all factors contribute to modifying the electronic and structural properties of the NCs, leading to these modifications in the bands.

3.3 UV-visible analysis

UV-visible spectroscopy was used to characterize the synthesized SZ-GO, N-GO, and S-GO and S3 presents the UV-visible spectra of GO, N-GO, and S-GO. GO exhibits two distinct absorption peaks at 230 nm and 300 nm, corresponding to the π–π* transition of C=C bonds in the aromatic ring and the n–π* transition of C=O bonds, respectively. In the spectra of S-GO and N-GO, the absorption peak shifts from 300 nm to 297 nm and 294 nm, respectively. This blue shift toward lower wavelengths suggests stronger bonding interactions, likely due to the removal of most oxygen-containing functional groups and the partial restoration of the conjugated C=C network, resulting in enhanced electron delocalization (Kashif *et al.*,[29] 2024).

Fig. 3 depicts the UV-visible spectra of Fe_2O_3/Ag_2O@GO, Fe_2O_3/Ag_2O@S-GO and Fe_2O_3/Ag_2O@N-GO NCs. The

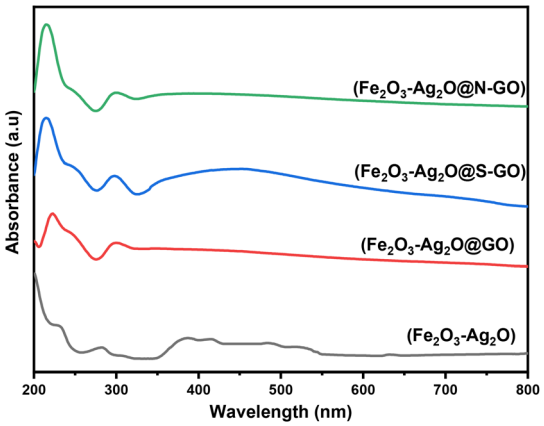

Fig. 3 UV-visible spectra of Fe_2O_3–Ag_2O, Fe_2O_3–Ag_2O@GO, Fe_2O_3–Ag_2O@S-GO and Fe_2O_3–Ag_2O@N-GO NCs.

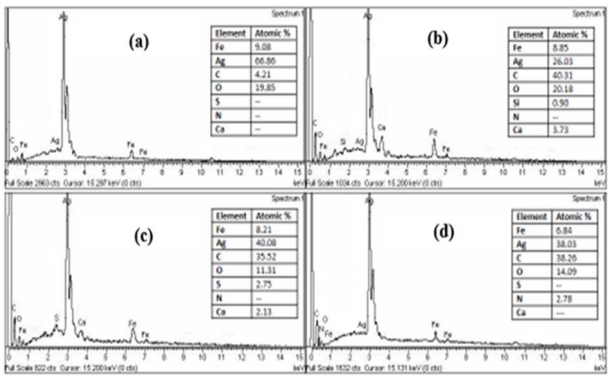

Fig. 4 EDX spectra for (a) Fe_2O_3–Ag_2O, (b) Fe_2O_3–Ag_2O@GO, (c) Fe_2O_3–Ag_2O@S-GO, (d) Fe_2O_3–Ag_2O@N-GO NCs.

absorption peaks were observed between 200 and 440 nm. The peak at 440 nm in Fe_2O_3/Ag_2O@S-GO confirmed the presence of Ag_2O in NCs, while the Fe_2O_3 exhibited a peak at 240 nm. The absorbance of Fe_2O_3/Ag_2O@GO NC revealed three prominent peaks between 200 and 350 nm, indicating the transformation of GO into Fe_2O_3/Ag_2O@GO nanoparticle. Fe_2O_3/Ag_2O@S-GO and Fe_2O_3/Ag_2O@N-GO displayed similar peaks to those of Fe_2O_3/Ag_2O@GO NC.

3.4 EDX analysis

EDX analysis was performed, and the corresponding elemental distributions are shown in S4. For the GO, only carbon and oxygen were detected, as presented in S4(A). In S-GO (S4(B)), sulfur was observed along with carbon and oxygen, confirming successful doping, with carbon remaining the predominant element. The presence of sulfur is attributed to the use of sodium sulfide as the doping agent. In the N-GO (S4(C)), nitrogen was detected alongside carbon and oxygen, confirming effective nitrogen incorporation. The presence of sulfur and nitrogen in their respective samples confirms the successful heteroatom doping of GO.

The EDX analyses of the synthesized Fe_2O_3–Ag_2O, Fe_2O_3–Ag_2O@GO, Fe_2O_3–Ag_2O@S-GO and Fe_2O_3–Ag_2O@N-GO NCs are shown in Fig. 4. In the synthesized NCs, the EDX spectrum documented that the assimilated metal oxide NCs were stoichiometric and comparable to ordinary configuration. The distinguishing X-ray peaks of the carbon, oxygen, sulphur, nitrogen, iron and silver atoms were visible in the spectrum of these NCs. All the respective constituent elements were present in the EDX spectra of the samples. In sample A, a carbon peak appeared, likely due to the use of carbon tape during the analysis. In samples B to D, the presence of carbon confirmed the incorporation of GO in all the NCs. In sample B, the atomic percentage of carbon was observed to be the highest, indicating a higher concentration of GO in this particular sample. Additionally, some contamination was evident in all the samples. This could be attributed to trace amounts of impurities in the precursor salts, environmental contamination, or other sources such as the experimental setup or handling during the synthesis process.

3.5 SEM analysis

Fig. 5(a–d) displays the SEM micrographs of Fe_2O_3–Ag_2O, Fe_2O_3–Ag_2O@GO, Fe_2O_3–Ag_2O@S-GO and Fe_2O_3–Ag_2O@N-GO NCs. Fig. 5(a) shows that the Fe_2O_3–Ag_2O NC exhibited close packing, leading to the formation of agglomerates. Particles were unevenly distributed, resulting in the formation of several cavities throughout the sample. Upon the incorporation of GO, the morphology of the sample changed significantly with a sheet- or flake-like structure observed, likely due to the presence of GO sheets. Closer observation revealed that the Fe_2O_3–Ag_2O NCs were unevenly distributed over the GO sheet. Additionally, N and S doping further altered the morphology of the samples. In case of pure GO incorporation, the granular morphology was replaced by sheets-like or flakes like structures, whereas in the case of S-GO the granular morphology was mostly retained with slight modifications. Due to agglomeration, individual grain boundaries were not visible, and the particles exhibited irregular shapes with many voids and porous structures.

3.6 Photocatalytic activity

The photocatalytic efficacy of Fe_2O_3–Ag_2O, Fe_2O_3–Ag_2O@GO, Fe_2O_3–Ag_2O@N-GO and Fe_2O_3–Ag_2O@S-GO NCs, synthesized through a hydrothermal method, was assessed, using methylene blue dye as the test substrate. The evaluation occurred in an outdoor setting under natural sunlight conditions. The gradual loss of the blue color over time signified the decolorization of the reaction mixture. After conducting UV-visible analysis using a double-beam spectrophotometer, there was an initial pronounced decrease observed in the absorbance maxima at 665 nm, indicating the degradation of the chromophore responsible for light absorption at that specific wavelength. Among all the prepared samples, Fe_2O_3–Ag_2O/S-GO NC displayed the highest photocatalytic activity. This increase in the activity attributed to the combination of enhanced charge separation, sulfur-induced active sites and optimized band

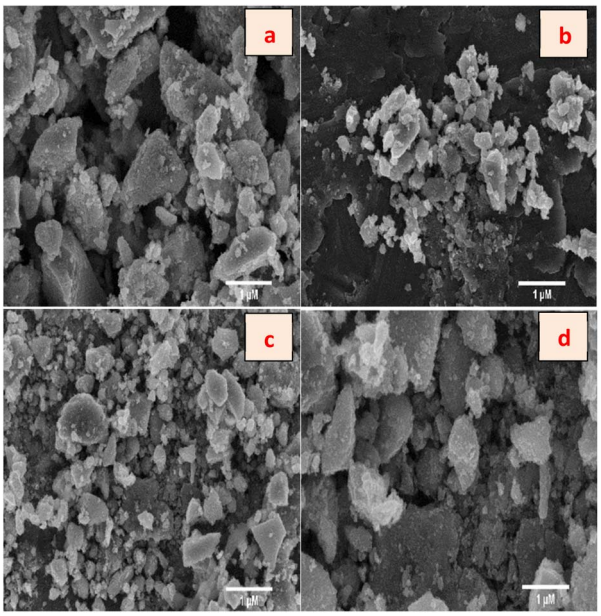

Fig. 5 (a–d) SEM images of Fe_2O_3–Ag_2O, Fe_2O_3–Ag_2O@GO, Fe_2O_3–Ag_2O@S-GO and Fe_2O_3–Ag_2O@N-GO NCs.

structure. The sulfur electron-donating nature (C–S–C) enriches GO's π-conjugated system, improving electron mobility enhancing the light absorption and this S-GO's conductive network rapidly shuttles electrons from Ag_2O's CB, leaving more h^+ for oxidation.[12]

When synthesized catalyst illuminated, the Fe_2O_3–Ag_2O NC effectively absorbs photons, generating electron–hole pairs. The excellent conductivity of GO, further enhanced by sulfur doping, rapidly accepts photogenerated electrons from the Fe_2O_3–Ag_2O NC, further suppressing electron–hole recombination and increasing the number of available charge carriers. Sulfur doping in GO can also induce defects and strong π–π interactions with the aromatic rings of MO facilitate significant adsorption of the dye molecules onto the catalyst surface, bringing the pollutant into close proximity with the reactive sites. The well-separated electrons then react with adsorbed O_2

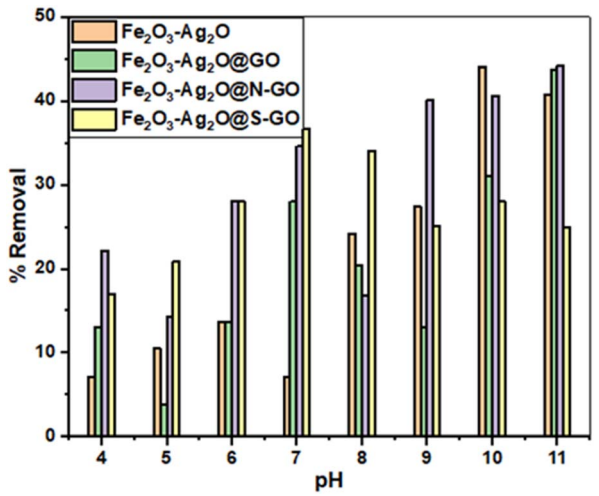

Fig. 6 Photocatalytic activity of Fe_2O_3–Ag_2O, Fe_2O_3–Ag_2O@GO, Fe_2O_3–Ag_2O@N-GO and Fe_2O_3–Ag_2O@S-GO NCs at different pH levels.

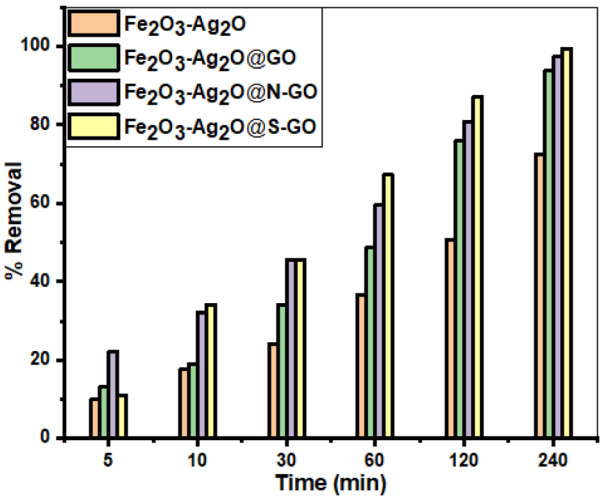

Fig. 7 Photocatalytic activity of Fe_2O_3–Ag_2O, Fe_2O_3–Ag_2O@GO, Fe_2O_3–Ag_2O@N-GO and Fe_2O_3–Ag_2O@S-GO NCs at different time intervals.

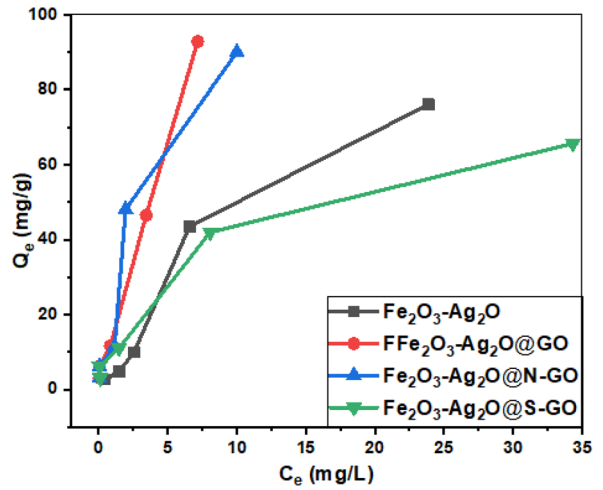

Fig. 8 Photocatalytic activity of Fe_2O_3–Ag_2O, Fe_2O_3–Ag_2O@GO, Fe_2O_3–Ag_2O@N-GO and Fe_2O_3–Ag_2O@S-GO NCs at different concentrations.

Table 1 Protein kinase inhibition potential of Fe_2O_3–Ag_2O, Fe_2O_3–Ag_2O@GO, Fe_2O_3–Ag_2O@N-GO and Fe_2O_3–Ag_2O@S-GO NCs

Samples	Bald zone (mm)	Clear zone (mm)
Fe_2O_3–Ag_2O	8 ± 0.02	11 ± 0.08
Fe_2O_3–Ag_2O@GO	9 ± 0.02	9 ± 0.03
Fe_2O_3–Ag_2O@N-GO	9 ± 0.01	7 ± 0.01
Fe_2O_3–Ag_2O@S-GO	8 ± 0.06	6 ± 0.05
Surfactin B	22.3 ± 0.04	—
DMSO	—	—

to produce superoxide radicals $^{\bullet}O_2^-$, while the holes react with H_2O/OH^- to generate highly oxidizing hydroxyl radicals ($^{\bullet}OH$). These ROS are the primary agents that subsequently attack and degrade the MB through a series of oxidative pathways, ultimately leading to their complete mineralization. The collective synergistic actions of efficient electron transfer, enhanced charge separation, increased light absorption, and improved pollutant adsorption driven by the Fe_2O_3–Ag_2O NCand the unique properties of S-GO lead to the significantly superior photocatalytic activity observed.[37–40]

3.7 Factors affecting the photocatalytic activity

3.7.1 Effect of pH. Fig. 6 depicts the photocatalytic activity of Fe_2O_3–Ag_2O, Fe_2O_3–Ag_2O@GO, Fe_2O_3–Ag_2O@N-GO and Fe_2O_3–Ag_2O@S-GO NCs. To optimize the best pH condition for efficient dye removal, dye degradation experiments were conducted at varying pH values ranging from 4 to 11. The pH of the dye solution was adjusted using 0.1 M NaOH and 0.1 M HCl. Dye degradation was observed under sunlight by applying a 20 mg catalyst and 0.1 M HCl. With an increase in pH, degradation proficiency improved, presumably due to the increased availability of hydroxide ions (OH^-), which facilitated the formation of reactive species essential for the photocatalytic process. The optimal pH was determined based on the maximum dye degradation rate observed. In Fe_2O_3–Ag_2O NC, degradation efficiency increased with increasing pH, with some deviations. It exhibited the lowest activity at 7 pH and the highest at 10 pH. Fe_2O_3–Ag_2O@GO NC showed irregular activity, with the lowest at pH 5 and the highest at 11 pH. Similarly, nitrogen and sulphur doped mixed metal GO NCs displayed irregular degradation activity.[41,42]

3.7.2 Effect of time. Fig. 7 displays the time study where 10 mL of dye solution was utilized along with 20 mg of catalyst. The reaction occurred under sunlight, with the dye concentration monitored over time through sample collection at various intervals. The dye degradation increased with time, reaching an optimal point, beyond which additional time did not significantly enhance degradation, suggesting the reaction's completion. This helped identify the optimal reaction time for achieving maximum degradation. All prepared samples *i.e.* Fe_2O_3–Ag_2O, Fe_2O_3–Ag_2O@GO, Fe_2O_3–Ag_2O@N-GO and Fe_2O_3–Ag_2O@S-GO NCs exhibited maximum activity at 240 min.[43,44]

3.7.3 Effect of concentration. Fig. 8 illustrates the concentration study, where varying initial concentrations of the dye solution were examined by using 20 mL of dye solution at different concentrations ranging from 12.5 to 200 mg L^{-1} along with a 20 mg of catalyst. As the dye concentration increased, the degradation efficiency decreased due to heightened competition for active sites on catalyst surface. Lower dye concentrations facilitated more efficient degradation, highlighting the importance of optimizing the initial dye concentration for efficient photocatalysis.[33]

3.8 Protein kinase inhibition potential

The tabulated (Table 1) results indicated that all NCs exhibited varying levels of protein kinase inhibition, ranging from

Table 2 MIC of nanocomposites against nonresistant and resistant bacterial strains

	Species	Activity & MIC (μg mL^{-1})	Fe_2O_3–Ag_2O	Fe_2O_3–Ag_2O@GO	Fe_2O_3–Ag_2O@N-GO	Fe_2O_3–Ag_2O@S-GO	Ciprofloxacin	DMSO
Non-resistant strains	*S. aureus*	Activity	Active	−ve	−ve	−ve	Active	−ve
		MIC	12.5				1.25	
	B. subtilis	Activity	−ve	−ve	−ve	−ve	Active	−ve
		MIC					1.25	
	K. pneumoniae	Activity	−ve	−ve	−ve	−ve	Active	−ve
		MIC					1.25	
	E. coli	Activity	−ve	−ve	−ve	−ve	Active	−ve
		MIC					1.25	
	P. aeruginosa	Activity	−ve	−ve	Active	Active	Active	−ve
		MIC			50	200	1.25	
Resistant strain	*Acinetobacter*	Activity					Active	
		MIC					1.25	
	E. coli	Activity	Active	−ve	−ve	Active	Active	−ve
		MIC	25			25	1.25	
	MRSA	Activity	−ve	−ve	−ve	Active	Active	−ve
		MIC				25	1.25	

Table 3 Antifungal potential evaluation of prepared nanocomposites

	Zone of inhibition (mm)				
Samples	*Mucor* sp. (mm)	*A. niger* (mm)	*A. flavus* (mm)	*A. fumigatus* (mm)	*F. solani* (mm)
Fe_2O_3–Ag_2O	7 ± 0.02	—	9 ± 0.02	—	—
Fe_2O_3–Ag_2O@GO	9 ± 0.01	9 ± 0.01	7 ± 0.02	6 ± 0.075	8 ± 0.05
Fe_2O_3–Ag_2O@N-GO	7 ± 0.02	6 ± 0.05	9 ± 0.01	7 ± 0.03	—
Fe_2O_3–Ag_2O@S-GO	9 ± 0.03	7 ± 0.02	8 ± 0.02	6 ± 0.02	9 ± 0.02
Amphotericin B	12 ± 0.05	12 ± 0.084	9 ± 0.02	10 ± 0.05	12 ± 0.06
DMSO	—	—	—	—	—

minimal to moderate, at the concentrations employed. All the samples exhibited a bald zone alongside a clear zone, indicating both bacteriostatic and bactericidal effects. The Fe_2O_3–Ag_2O NC demonstrated a notable effect, achieving a maximum zone of inhibition of 11 ± 0.08 mm. The presence of Ag in these NCs may have contributed to this inhibitory activity.[45]

3.9 Antibacterial potential

The antibacterial activities of Fe_2O_3–Ag_2O, Fe_2O_3–Ag_2O@GO, Fe_2O_3–Ag_2O@N-GO, and Fe_2O_3–Ag_2O@S-GO NCs against both non-resistant and resistant bacterial strains are presented in the Table 2. The findings indicated that Fe_2O_3–Ag_2O NC, devoid of GO, exhibited activity against *S. aureus* with an MIC of 12.5 μg mL^{-1}. In contrast, Fe_2O_3–Ag_2O@N-GO and Fe_2O_3–Ag_2O@S-GO NCs, demonstrated activity against *Pseudomonas aeruginosa*; however, with higher MIC values of 200 μg mL^{-1}. For resistant bacterial strains, Fe_2O_3–Ag_2O NC (without GO) demonstrated activity against *Escherichia coli*, exhibiting an MIC of 25 μg mL^{-1}. Fe_2O_3–Ag_2O@S-GO exhibited activity against *Acinetobacter* and *Escherichia coli*, with an MIC of 25 μg mL^{-1}. These results suggested that Fe_2O_3–Ag_2O NC possessed enhanced antibacterial properties.[46,47]

3.10 Antifungal activity

The antifungal activity of prepared nanocomposites was evaluated against five fungal species. The results indicated that all NCs exhibited mild to moderate antifungal activity against the tested strains, except for Fe_2O_3–Ag_2O NC, which demonstrated antifungal activity only against *Mucor* sp. Among all the NCs, Fe_2O_3–Ag_2O@GO NC displayed the most significant antifungal activity against all strains, with the highest effectiveness against *Aspergillus niger* and *Mucor*, achieving a zone of inhibition of 9 ± 0.01 mm (Table 3).[48,49]

Table 4 Percentage hemolytic activity of nanocomposites against red blood cells

Nanocomposites code	% hemolysis ± SD
Fe_2O_3–Ag_2O	0.54 ± 0.53
Fe_2O_3–Ag_2O@GO	0.43 ± 0.22
Fe_2O_3–Ag_2O@N-GO	0.87 ± 0.24
Fe_2O_3–Ag_2O@S-GO	0.38 ± 0.17
Triton X	100
Phosphate buffer saline	—

3.11 Hemolytic activity

The hemolytic assay of the NCs was conducted to evaluate their hemocompatibility with red blood cells (Table 4). If the samples exhibited low to no hemolysis at the specified concentration, it indicates their non-toxicity and potential suitability for human use in formulated product. The tabulated results indicated that all the NCs exhibited hemolysis levels below 1%, confirming their safety for use.[16]

4. Conclusions

In this study, Fe_2O_3–Ag_2O, Fe_2O_3–Ag_2O@GO, Fe_2O_3–Ag_2O@N-GO, and, Fe_2O_3–Ag_2O@S-GO NCs were prepared by the hydrothermal method. This method offers controlled morphology, high purity, scalability, eco-friendliness, and efficient doping, making it ideal for synthesizing advanced nanomaterials. The physicochemical analyses revealed that the crystallinity and morphology were significantly affected by the interaction among bimetal oxides, graphene oxide, and nitrogen- and sulfur-doped GO. The incorporation of nitrogen- and sulfur-doped GO enhanced the photocatalytic efficiency of the NCs against MB dye. The optimization process indicated that the pH, time, and dye concentration significantly influenced the photocatalytic process. Both, bacteriostatic and bactericidal, effects were shown by all samples. Moreover, inhibitory effects against both resistant and non-resistant bacterial strains were also observed. GO doped NC displayed the highest antifungal activity while hemolytic assay confirmed the safety of all NCs for biological applications. These findings make these NCs promising candidates for photocatalysis and biological applications to achieve the sustainable development goals.

Author contributions

Safeena Zafar: formal analysis and writing – original draft; Bilal Ahmad Khan: supervision, project administration, conceptualization, methodology and project administration; Ikhtiar Ahmad and Aroosa Zafar: visualization, and writing – original draft; Muhammad Naeem Ahmed and Rasool Khan: software,

visualization and data curation; Sirajul Haq and Mahmoud A. A. Ibrahim: validation and writing – review & editing.

Conflicts of interest

There are no conflicts to declare.

Data availability

All relevant experimental details and raw data, including characterization results (XRD, SEM, EDX, FTIR, and UV-vis) and photocatalytic activity measurements, have been archived and can be accessed by request. Beside this, the biological applications *i.e.* combating microbial infections, inhibiting cancer-related protein kinases, and assessing biocompatibility through hemolytic analysis. Due to the large amount of data related to the calculation results in this paper and the limitation of the data sharing conditions of our institution, it is not possible to upload all the data to the public network, so we disclose the relevant calculation script files involved in the research process.

The data that support the findings of this study are available from the corresponding author upon reasonable request.

Any additional information regarding the materials and methods used in this study can also be provided upon request to support further inquiries and reproduction of results.

The supplementary files includes the XRD, FTIR, UV-vis and EDX spectra of GO (SZ-GO), S-GO (SZ-GS) and N-GO (SZ-GN). See DOI: **https://doi.org/10.1039/d5ra05475c**.

References

1 R. Y. Smith, A. Kar and V. Subramanian, *Ind. Eng. Chem. Res.*, 2019, **48**, 10268–10276.
2 L. Zhang, F. Lv, W. Zhang, R. Li, H. Zhong, Y. Zhao, Y. Zhang and X. Wang, *J. Hazard. Mater.*, 2009, **171**, 294–300.
3 M. Farhan Hanafi and N. Sapawe, *Mater. Today: Proc.*, 2020, **31**, A141–A150.
4 G. Zhang, X. Zhang, Y. Meng, G. Pan, Z. Ni and S. Xia, *Chem. Eng. J.*, 2019, 123684.
5 C. Lin, H. Liu, M. Guo, Y. Zhao, X. Su, P. Zhang and Y. Zhang, *Colloids Surf., A*, 2022, **646**, 128962.
6 K. Ravichandran, N. Chidhambaram and S. Gobalakrishnan, *J. Phys. Chem. Solids*, 2016, **93**, 82–90.
7 S. Singh, A. G. Anil, S. Khasnabis, V. Kumar, B. Nath, V. Adiga, T. S. S. Kumar, S. Subramanian, V. Kumar, J. Singh and P. C. Ramamurthy, *Environ. Res.*, 2022, **203**, 111891.
8 P. Shengyan, Z. Rongxin, M. Hui, D. Daili, P. Xiangjun, Q. Fei and C. Wei, *Appl. Catal., B*, 2017, **218**, 208–219.
9 Z. Durmus, Z. Kurt and A. Durmus, *ChemistrySelect*, 2019, **4**, 271–278.
10 S. S. Wagh, C. V. Jagtap, V. S. Kadam, S. F. Shaikh, M. Ubaidullah, B. Pandit, D. B. Salunkhe and R. S. Patil, *ES Energy Environ.*, 2022, **17**, 94–105.
11 M. Khan, M. N. Tahir, S. F. Adil, H. U. Khan, M. R. H. Siddiqui, A. A. Al-Warthan and W. Tremel, *J. Mater. Chem. A*, 2015, **3**, 18753–18808.
12 C. Kuang, P. Tan, M. Javed, H. H. Khushi, S. Nadeem, S. Iqbal, F. H. Alshammari, M. D. Alqahtani, H. O. Alsaab and N. S. Awwad, *Inorg. Chem. Commun.*, 2022, **141**, 109575.
13 S. Prabhu and E. K. Poulose, *Int. Nano Lett.*, 2012, **2**, 32.
14 A. Hoppe, N. S. Güldal and A. R. Boccaccini, *Biomaterials*, 2011, **32**, 2757–2774.
15 Z. Yarjanli, K. Ghaedi, A. Esmaeili, S. Rahgozar and A. Zarrabi, *BMC Neurosci.*, 2017, **18**, 1–12.
16 M. Haris, N. Fatima, J. Iqbal, W. Chalgham, A. S. Mumtaz, M. A. El-Sheikh and M. Tavafoghi, *Molecules*, 2023, **28**, 2091.
17 M. Shahzad Shirazi, M. Moridi Farimani, A. Foroumadi, K. Ghanemi, M. Benaglia and P. Makvandi, *Sci. Rep.*, 2022, **12**, 1–15.
18 T. Iqbal, A. Hassan and S. Ghazal, *Int. J. Sci. Eng. Res.*, 2016, **7**, 1178–1221.
19 J. Chiou, B. Lai, K. Hsu and D. Chen, *J. Hazard. Mater.*, 2013, **248–249**, 394–400.
20 N. Ibrayev, A. Nuraje, G. Amanzholova, E. Seliverstova and T. Khamza, *Eng. Sci.*, 2023, **26**, 1–11.
21 T. P. Mokoena, H. C. Swart and D. E. Motaung, *J. Alloys Compd.*, 2019, **805**, 267–294.
22 S. Sahoo, S. Bae, Y. Lee, J. Lee, J. Ahn, C. Kim and I. Oh, *Carbon*, 2015, **94**, 455–463.
23 S. P. Dubey, T. T. M. Nguyen, Y. Kwon and C. Lee, *J. Ind. Eng. Chem.*, 2015, **29**, 282–288.
24 S. Zafar, B. A. Khan, I. Ahmad, M. N. Ahmed, A. Zafar, R. Khan, M. A. El-Tayeb, A. M. Awad, T. Shoeib and M. A. A. Ibrahim, *Chem. Phys. Impact*, 2024, **9**, 100748.
25 (*a*) S. Kolarević, D. Milovanović, M. Avdović, M. Oalde, J. Kostić-Vuković, K. Sunjog, B. Nikolić, J. Knezevic-Vukcević and B. Vukovic-Gacic, *Bot. Serbica*, 2016, **40**, 29–36; (*b*) S. Zafar, B. A. Khan, I. Ahmad, M. N. Ahmed, A. Zafar, R. Khan, M. A. El-Tayeb, A. M. Awad, T. Shoeib and M. A. A. Ibrahim, *Chem. Phys. Impact*, 2024, **9**, 100748.
26 (*a*) L. Q. Chen, L. Fang, J. Ling, C. Z. Ding, B. Kang and C. Z. Huang, *Chem. Res. Toxicol.*, 2015, **28**, 501–509; (*b*) N. Kumar and M. Samarpita, *Appl. Water Sci.*, 2020, **10**, 1–10.
27 K. Aftab, T. Naseem, S. Hussain, S. Haq, M. U. Rehman and M. Waseem, *Environ. Sci. Pollut. Res.*, 2023, **30**(2), 4079–4093.
28 W. Fan, W. Gao, C. Zhang, W. W. Tjiu, J. Pan and T. Liu, *J. Mater. Chem.*, 2012, 25108–25115.
29 H. Kashif, M. N. Ahmed, M. Altaf, I. ul Haq, A. Iqbal and S. Haq, *Microsc. Res. Tech.*, 2024, **87**, 1479–1493.
30 D. Zhao, X. Gao, C. Wu, R. Xie, S. Feng and C. Chen, *Appl. Surf. Sci.*, 2016, **384**, 1–9.
31 J. Ahmad and K. Majid, *Polym. Bull.*, 2021, **78**, 3889–3911.
32 M. Iqbal, Z. U. Abdin, T. Naseem, M. Waseem, S. U. Din, M. Hafeez, S. Haq, S. Qureshi, A. Bibi, S. U. Rehman and R. Hussain, *J. Inorg. Organomet. Polym. Mater.*, 2021, **31**, 100–111.
33 (*a*) R. Vinayagam, R. Selvaraj, P. Arivalagan and T. Varadavenkatesan, *J. Photochem. Photobiol., B*, 2020, **203**, 111760; (*b*) A. Hamid, S. Haq, S. Ur Rehman, K. Akhter, W. Rehman, M. Waseem, S. Ud Din, Z. U. Abdin,

M. Hafeez, A. Khan and A. Shah, *Chem. Pap.*, 2021, **75**, 4189–4198; (*c*) N. Bibi, S. Haq, W. Rehman, M. Waseem, M. U. Rehman, A. Shah, B. Khan and P. Rasheed, *Biointerface Res. Appl. Chem.*, 2020, **10**, 5895–5900; (*d*) S. Haq, W. Rehman, M. Waseem, V. Meynen, S. U. Awan, S. Saeed and N. Iqbal, *J. Photochem. Photobiol., B*, 2018, **186**, 116–124.

34 A. Ragunathan, R. Krishnan and B. Ameen, *J. Chem. Res.*, 2015, **39**, 622–626.

35 S. N. Basahel, M. Mokhtar, T. T. Ali and K. Narasimharao, *Catal. Today*, 2020, **348**, 166–176.

36 (*a*) R. B. Anjaneyulu, B. S. Mohan, G. P. Naidu and R. Muralikrishna, *Phys. E*, 2019, **108**, 105–111; (*b*) H. Kashif, M. N. Ahmed, M. Altaf, I. ul Haq, A. Iqbal and S. Haq, *Microsc. Res. Tech.*, 2024, **87**, 1479–1493.

37 Y. Cui, H. Sun and P. Guo, *Nanotechnology*, 2020, **31**, 245702.

38 W. Zhou, H. Liu, J. Wang, D. Liu, G. Du and J. Cui, *ACS Appl. Mater. Interfaces*, 2010, **2**, 2385–2392.

39 D. Sarkar, C. K. Ghosh, S. Mukherjee and K. K. Chattopadhyay, *ACS Appl. Mater. Interfaces*, 2013, **5**, 331–337.

40 Y. Cui, J. Briscoe, Y. Wang, N. V. Tarakina and S. Dunn, *ACS Appl. Mater. Interfaces*, 2017, **9**, 24518–24526.

41 S. Haq, R. Ehsan, F. Menaa, N. Shahzad, S. U. Din, M. I. Shahzad, W. Rehman, M. Waseem, W. Alrhabi, H. A. Almukhlifi and S. A. Alsharef, *Catalysts*, 2022, **12**, 1397–1403.

42 M. S. H. Bhuiyan, M. Y. Miah, S. C. Paul, T. Das Aka, O. Saha, M. M. Rahaman, M. J. I. Sharif, O. Habiba and M. Ashaduzzaman, *Heliyon*, 2020, **6**, e04603.

43 O. C. Olatunde and D. C. Onwudiwe, *J. Inorg. Organomet. Polym. Mater.*, 2022, **32**, 2578–2590.

44 S. Kaushal, A. Kumar, H. Bains and P. P. Singh, *Environ. Sci. Pollut. Res.*, 2023, **30**, 37092–37104.

45 S. Iravani and R. S. Varma, *Green Chem.*, 2020, **22**, 2643–2661.

46 S. Haq, M. Rashid, F. Menaa, N. Shahzad, M. Imran Shahzad, S. Y. M. Alfaifi, O. Madkhali, M. D. Aljabri, M. Ashravi, R. A. Tayeb and M. M. Rahman, *Arabian J. Chem.*, 2023, **16**, 104917.

47 Z. Hashemi, Z. M. Mizwari, S. R. Alizadeh, M. Habibi, S. Mohammadrezaee, S. M. Ghoreishi, S. Mortazavi-Derazkola and M. A. Ebrahimzadeh, *Inorg. Chem. Commun.*, 2023, **154**, 110982.

48 M. Hasanin, A. H. Hashem, I. Lashin and S. A. M. Hassan, *Biomass Convers. Biorefin.*, 2023, **13**, 8865–8875.

49 S. Haq, N. Shahzad, M. I. Shahzad, K. Elmnasri, M. Ben Ali, A. Baazeem, A. Hedfi and R. Ehsan, *Molecules*, 2022, **27**(19), 6750.